Volume 1 | Number 1 | Jan 2013 | Pages 1–100

Dalton Transactions

An international journal of inorganic chemistry
www.rsc.org/dalton

ROYAL SOCIETY OF CHEMISTRY

ROYAL SOCIETY OF CHEMISTRY

www.rsc.org/dalton

ARTICLE TYPE

One-pot controlled synthesis of sea-urchin shaped Bi$_2$S$_3$/CdS hierarchical heterostructures with excellent visible light photocatalytic activity

Yunhan Shi,[a] Yajie Chen,[a] Guohui Tian,*[a,b] Honggang Fu,[a] Kai Pan,[a] Juan Zhou[a] and Haijing Yan[a]

In this study, sea-urchin shaped Bi$_2$S$_3$/CdS hierarchical heterostructures are successfully synthesized via a convenient one-pot growth rate controlled route. The product is mainly composed of Bi$_2$S$_3$ nanorods and CdS nanoparticles grown on their surfaces. The formation mechanism was

10 proposed based on the evolution of morphology as a function of solvothermal time, which involves the fast formation of initial sea-urchin shaped Bi$_2$S$_3$ nanoflowers, followed by the gradual growth of numerous CdS nanoparticles on Bi$_2$S$_3$ nanoflowers. The effects of CdS in the composites on the microstructures, optical absorption properties, and photocatalytic activity were investigated comparatively. Due to the synergetic effects between hierarchical Bi$_2$S$_3$ nanoflowers and CdS

15 nanoparticles, the obtained Bi$_2$S$_3$/CdS hierarchical heterostructures exhibit superior catalytic activity over the independent components. Furthermore, the obtained Bi$_2$S$_3$/CdS hierarchical heterostructure composite show strongly structure-induced enhancement of photocatalytic performance for the photodegradation of Rhodamine B.

20 1. Introduction

Recent years, semiconductor photocatalysts with unique shape and structures have received much attention and could offer many opportunities and challenges in photocatalysis. However, a single component photocatalyst is unlikely to satisfy all the

25 critical requirements. Fortunately, the heterojunctional composites with multiple integrated functional components could combine the advantages of different components to overcome some drawbacks of single component photocatalysts.[1] It has been demonstrated in photocatalysis that junction semiconductors

30 show greatly enhanced activities compared to a single semiconductor due to the enhanced photogenerated electron-hole separation rate.[2] In the past few years, nanoparticle composites were widely studied and showed enhanced photcatalytic activity because carriers migrating to the surface have favourably shorted

35 distances to travel.[3] However, carriers migration requires a suitable concentration gradient or potential gradient from one component to the other one, which is closely correlated with the morphology, structure and surface properties of nanostructured materials.[4,5] In recent years, great progress has been achieved in

40 the shape-controlled synthesis of photocatalytic materials and investigations of the relationship between the morphological (or structural) characteristics and the photocatalytic properties.[6] For example, 1D heterostructures have received prodigious interest because of their synergetic effects on photocatalytic

45 performance.[7-9] Especially, great emphasis has been placed on hierarchical heterostructures for facilitating the separation of photogenerated electron-hole pairs in order to further enhance the photocatalytic activity. In semiconductor-semiconductor

composite hierarchical nanostructures, both types of

50 semiconductors can undertake the task of harvesting incident photons. Synergetic effects on both carrier separation and photocatalytic efficiency in such nanostructures have been extensively studied in recent years.[10-12] In most cases, a narrow bandgap semiconductor serves as a visible light sensitizer to

55 transfer the excited-state electrons to a large bandgap semiconductor.[13-15] Recently, heterojunction composites composed of two narrow bandgap semiconductors have attracted more attention in photocatalytic applications due to their extended and enhanced visible light properties.[16-18]

60 During the past decades, chalcogenide semiconductors have attracted much attention in the solar energy conversion and environmental management due to their visible light absorption, unique size-dependent physical and chemical properties.[19-21] Among the photocatalysts under investigation, CdS is a good

65 candidate semiconductor for its excellent light absorption property in the visible region.[22-25] Moreover, the component of CdS is less expensive and the preparation method of CdS is relatively simple, which makes the CdS-based photocatalyst a more suitable choice compared with other photocatalysts for

70 fundamental understanding.[26] Bi$_2$S$_3$ is an attractive material due to its good conductivity, thermoelectric properties and narrow band-gap (1.3 eV). Bi$_2$S$_3$ has attracted considerable attention for its potential applications in many areas including photocatalysis.[27-29] So far, Bi$_2$S$_3$ nanostructures, including simple

75 one-dimensional (1D) nanostructures such as nanorods, nanowires and nanotubes, some complex nanostructures, such as two-dimensional (2D) and three-dimensional (3D) nanostructures including network-like and flower-like structures have been

synthesized by various of methods.[30-34] However, the application of Bi_2S_3 or CdS in photocatalysis is often limited because the quick photogenerated carriers recombination and the relatively low visible light photocatalytic activity. It is meaningful to combine both advantages of the CdS and Bi_2S_3 materials in light harvesting and electron transfer and construct Bi_2S_3/CdS heterojunction composites.[35] Recently, Fang et al. synthesized Bi_2S_3/CdS 1D nanowire/nanoparticle heterostructures through an epitaxial growth pathway in liquid phase and explore their photocatalytic application.[36] There are no reports of the hierarchical Bi_2S_3/CdS heterostructure, although hierarchical heterostructures can significantly enhance the photocatalytic activity due to their special morphology and structure characteristics. Generally, the fabrication of the hierarchical heterostructure composites usually based on two steps and complicated reactions. The hierarchical structural supporter is first prepared, and then coated with another semiconductor to form hierarchical composite. Therefore, how to construct Bi_2S_3/CdS hierarchical heterostructures via a facile one-spot route is still a significant challenge.

In this paper, we reported a facile one-pot growth rate controlled route for the synthesis of sea-urchin shaped Bi_2S_3/CdS hierarchical heterostructures by a hydrothermal process. In this process, consecutive reactions of the sulfur source with Bi and Cd salts led to the formation of sea-urchin shaped Bi_2S_3/CdS hierarchical heterostructures due to their significantly different reaction rates. It avoided the extreme reaction conditions and the assistance of template or surfactants. To confirm the advantage of the unique hierarchical heterojunction, the photocatalytic controlled experiments were taken on the photocatalytic degradation of Rhodamine B under visible light irradiation using the as-prepared samples.

2. Experimental section

2.1. Synthesis of sea-urchin shaped Bi_2S_3/CdS hierarchical heterostructures

In a typical experiment, 3 mmol thiourea, 0.1 mmol $Cd(NO_3)_2 \cdot 4H_2O$, 0.2 mmol $Bi(NO_3)_3 \cdot 5H_2O$ were dissolved in a mixture of 20 mL of ethanol and 7 mL of glycerol. The mixed aqueous solution was transferred to a Teflon-lined stainless-steel autoclave with a capacity of 40 mL. The sealed autoclave was heated at 150 °C for 10 h in an oven. After reaction, the autoclave was cooled naturally. The final black solid product was centrifuged, washed with anhydrous ethanol several times, and finally vacuum-dried at 60 °C for 2 h. To further understand the influence of CdS content on enhancing the photcatalytic activity and morphology change, keeping other synthetic conditions unchanged, a different amount of $Cd(NO_3)_2 \cdot 4H_2O$ was added to change the molar ratios of Bi^{3+} to Cd^{2+} at 5:1, 3:1, 2:1 and 1:1. The resulting samples were labeled as BC5, BC3, BC2 and BC1, respectively. For comparison, bare CdS and Bi_2S_3 were obtained under the same experimental conditions in the absence of $Bi(NO_3)_3 \cdot 5H_2O$ and $Cd(NO_3)_2 \cdot 4H_2O$, respectively.

2.2. Characterization

The X-ray diffraction (XRD) of powder samples was examined on a Bruker D8 Advance diffractometer using Cu Ka radiation (l = 0.15405 nm, 40 kV, 100 mA). Transmission electron microscopy (TEM) and high-resolution TEM (HRTEM) images of samples were recorded in a JEOL 2100 microscope with a 200 kV accelerating voltage, scanning electron microscopy (SEM, Hitachi, S-4800). The surface elements and their electronic states of the samples were analyzed using X-ray photoelectron spectroscopy (XPS, Kratos-AXIS UL TRA DLD, Al Ka X-ray source). The UV-visible diffuse reflectance spectra of the samples were obtained using a UV-visible spectro-photometer (Shimadzu UV-2550).

2.3. Measurement of photocatalytic activity.

The photodegradation experiments were performed in a slurry reactor containing 0.1 g of catalyst, 50 mL of Rhodamine B solution (10 mg/L, RhB). A 150 W Xe lamp was used as a light source, and a 420 nm cutoff filter was used to cut off UV light. Prior to irradiation, the suspension was kept in the dark under stirring for 60 min to ensure the establishing of an adsorption/desorption equilibrium. At given time intervals, 2 mL aliquots were collected from the suspension and immediately centrifuged, the concentration of RhB after illumination was determined at 554 nm using a UV–vis spectrophotometer (Shimadzu UV-2550). After the measurement, the sampled RhB solution was returned to the reactor to make sure the total volume of the reaction solution is unchanged. In order to detect the active species during the photocatalytic reaction, hydroxyl ($^\bullet$OH) radicals produced by the photocatalysts under visible light irradiation were measured by the fluorescence method on a Fluoromax-4 Spectrophotometer (Horiba Jobin Yvon) using terephthalic acid (TA) as a probe molecule. The $^\bullet$OH radical trapping experiments were carried out using the following procedure: A 5 mg portion of the sample was dispersed in 30 mL of a 5×10^{-4} M TA aqueous solution in a diluted NaOH aqueous solution (2×10^{-3} M). The resulting suspension was then exposed to visible light irradiation for 20 min. 2 mL of the suspension was collected and centrifuged to measure the maximum fluorescence emission intensity with an excitation wavelength of 315 nm. A total organic carbon (TOC) analyzer (AnalytikJena, Multi N/C 2100S, Germany) was employed for mineralization degree analysis of the dye solutions. Prior to injection into the TOC analyzer, the samples were filtrated with a 0.45 ím Millipore filter. All experiments were carried out at least in duplicate. The reported values were within the experimental error range of ±3%.

3. Results and discussion

The crystal structures of the three different products were verified by XRD characterization, as shown in Fig. 1. The X-ray diffraction patterns of a and c shown in Fig. 1 revealed the presence of pure orthorhombic phase Bi_2S_3 (JCPDS card No.17-0320) and the hexagonal phase CdS (JCPDS Card No. 41-1049), respectively.[35] The XRD pattern of the CdS/Bi_2S_3 heterostructure is shown in Fig. 1 b, besides the diffraction peaks corresponding to the Bi_2S_3 mother nanocrystals, the other peaks can be assigned to the characteristic reflection of (002) plane of hexagonal phase CdS (the diffraction peak highlighted with the asterisk ★). The relatively weak diffraction peak of CdS is due to the limited CdS loading in the heterostructures and the partial diffraction peaks overlap with those of the Bi_2S_3.
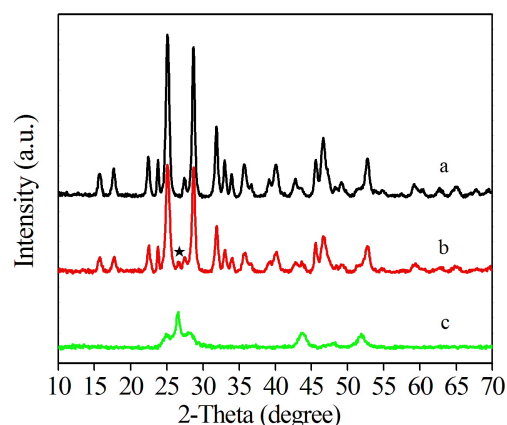
Fig. 1 XRD patterns of the as-obtained Bi_2S_3 (a), Bi_2S_3/CdS heterostructures (b), and CdS (c).
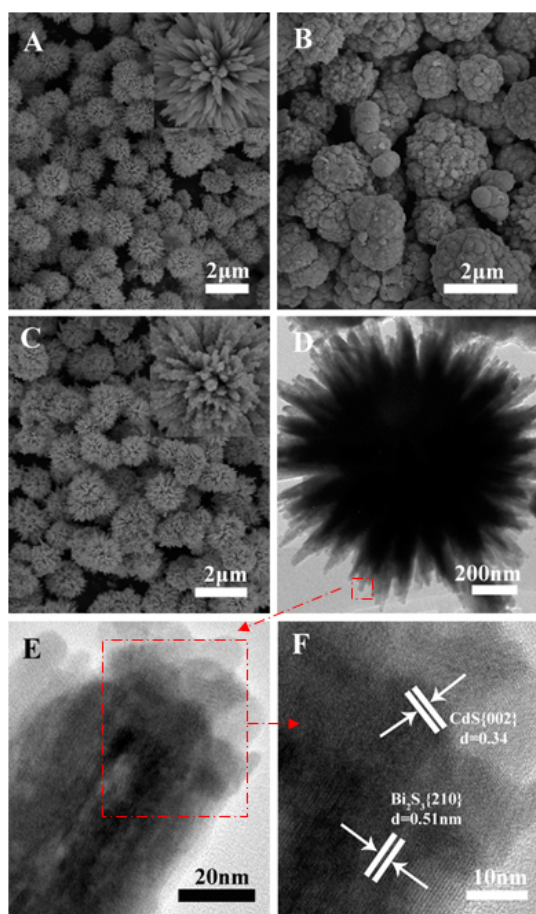
5 **Fig. 2** SEM images of the Bi_2S_3 (A), CdS (B) and Bi_2S_3/CdS heterostructure (C); TEM (D, E) and HRTEM (F) images of the Bi_2S_3/CdS heterostructure (BC2).

To further examine the formation of Bi_2S_3/CdS heterostructure
10 composites, the morphology and microstructure of the different products were investigated with electron microscopy. Fig. 2A-C show the SEM images of different products. We can find that pure Bi_2S_3 (Fig. 2A) is sea-urchin shaped morphology composed of nanorods (inset of Fig. 2A). The morphology of pure CdS (Fig.
15 2B) is uneven size nanospherical, which is gathered by CdS nanoparticles. From Fig. 2C, especially from the enlarged single sea-urchin shaped Bi_2S_3/CdS hierarchical heterostructure in the

inset of Fig. 2C, we can clearly observe that numerous CdS nanoparticles have grown on the surface of Bi_2S_3 nanoflowers.
20 The size of the single sea-urchin shaped Bi_2S_3/CdS hierarchical heterostructure is about 1.5 μm (Fig. 2D-F), which consisted of numerous nanorods. The diameter of nanorods is about 40~50 nm, and many CdS nanoparticles grew on their surface (Fig. 2E). From the Fig. 2F, it can be estimated that the average CdS
25 nanoparticle size is about 8 nm. Furthemore, there are two different lattice fringes in HRTEM image. The interplanar spacing of 0.29 nm corresponds to the (210) plane of Bi_2S_3, while 0.34 nm corresponds to the (002) plane of hexagonal phase CdS. So the growth direction of Bi_2S_3 nanorods can be indexed to the
30 reflection along the [210] direction. So it can demonstrate that CdS nanoparticles successfully grow on the surface of Bi_2S_3 nanoflowers, implying the formation of Bi_2S_3/CdS heterostructure.


35
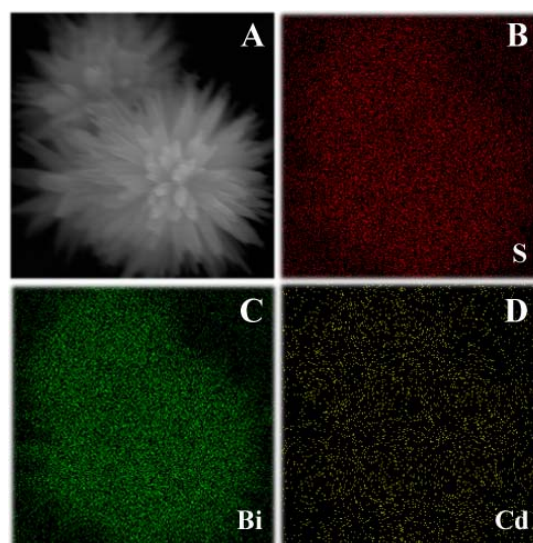
Fig. 3 SEM image (A) of the sea-urchin shaped Bi_2S_3/CdS hierarchical heterostructure (BC2) and the corresponding EDS mapping of S (B, red), Bi (C, green) and Cd (D, yellow).

40 To further accurately investigate the nanoscale elemental composition as well as the spatial uniformity of the elemental distribution, X-ray energy dispersive spectrometry (EDS) was carried out on single sea-urchin shaped Bi_2S_3/CdS hierarchical heterostructure (Fig. 3). The EDS mapping images indicate the
45 coexistence and homogeneous distribution of S, Bi and Cd elements among the whole Bi_2S_3/CdS hierarchical nanoflower architectures. Moreover, Cd element surface content is about 32.8 at%, which is lower than that of the other two elements. The element mapping images also revealed the formation of
50 heterogeneous structure of Bi_2S_3/CdS.

X-ray photoelectron spectroscopy (XPS) was used to investigate the surface valence state and the chemical composition of hierarchical Bi_2S_3/CdS heterostructure. As shown in Fig. 4A, the product is mainly composed of Bi, Cd and S
55 elements (C signals come from the reference sample). The oxygen peak (532.0 eV) may be attributed to O_2 or H_2O adsorbed onto the samples from the atmosphere. High-resolution scans of the S element in Fig. 4B reveal several weak peaks centered at around 160.5 and 159.5, which can be accordingly assigned to

binding energies of S2p$_{3/2}$. High-resolution scan of the S element in Fig. 4D is attributed to the S2s. The results prove the existence of the S^{2+} species. Moreover, the high-resolution XPS spectra (Fig. 4B, C) show that the binding energies of Bi4f$_{7/2}$, Bi4f$_{5/2}$, S2p, Cd3d$_{3/2}$ and Cd3d$_{5/2}$ peaks in the pure Bi$_2$S$_3$ and CdS are located at 158.0 eV, 163.2 eV, 160.5 eV, 405.0 eV and 412.0 eV, respectively.[37,38] According to the results of the XPS, for the Bi$_2$S$_3$/CdS hierarchical heterostructure, the peaks corresponding to Bi4f$_{7/2}$, Bi4f$_{5/2}$, S2p, Cd3d$_{3/2}$ and Cd3d$_{5/2}$ shifted to 157.0, 162.3, 159.5, 404.0 and 411.0 eV, respectively. The slight shift to the lower energy direction of the peaks can be attributed to the interaction between Bi$_2$S$_3$ and CdS in the composite, suggesting the formation of the heterostructure between the CdS nanoparticles and Bi$_2$S$_3$ nanoflowers.
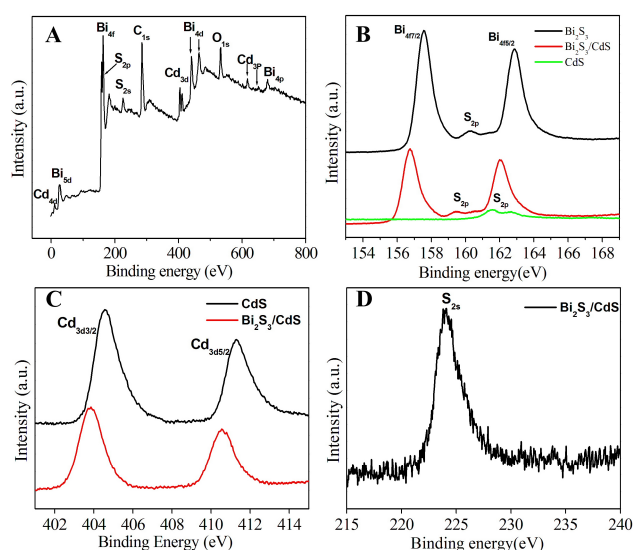

Fig. 4 Survey XPS spectrum of Bi$_2$S$_3$/CdS heterostructure (A), High-resolution XPS spectrum of Bi4f (B), S2p (B) and Cd3d peaks (C) of the different samples, High-resolution XPS spectrum of S2s of Bi$_2$S$_3$/CdS heterostructure.
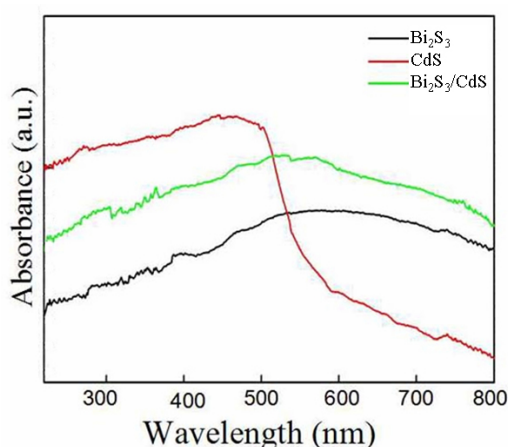
Fig. 5 UV-visible absorption spectra of the different samples: Bi$_2$S$_3$, CdS and Bi$_2$S$_3$/CdS.

Fig. 5 describes UV-visible diffuse-reflectance spectroscopy (UV-vis DRS) of CdS, Bi$_2$S$_3$ and Bi$_2$S$_3$/CdS heterostructures. A wide absorption across the visible light

spectrum was observed for Bi$_2$S$_3$. The absorption spectrum of the Bi$_2$S$_3$/CdS composite is similar to that of Bi$_2$S$_3$. But the enhanced absorption spectrum intensity was observed for the Bi$_2$S$_3$/CdS composite compared with the spectrum of the Bi$_2$S$_3$. This should be attributed to the synergistic effect of the two compositions and the large absorption of CdS at wavelengths lower than 600 nm. So we have reason to believe that this photocatalyst with a strong visible light wavelength absorption band is an attractive photocatalyst for pollutant degradation.
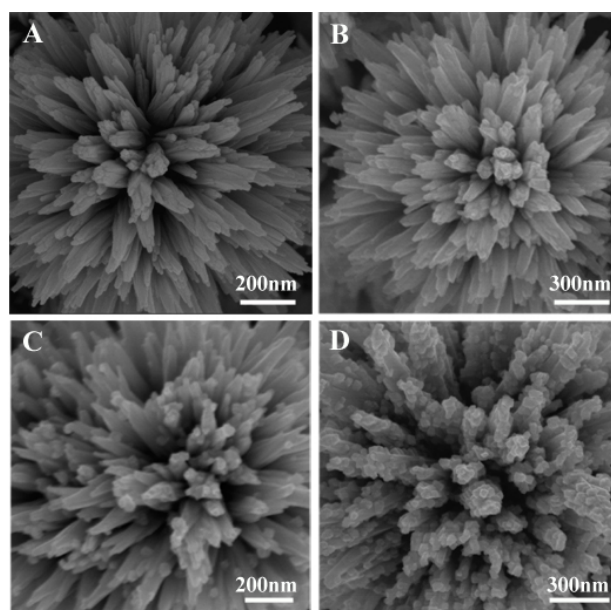

Fig. 6 SEM images of Bi$_2$S$_3$/CdS composites obtained from the different reaction time: 5 min (A), 1 h (B), 3 h (C) and 10 h (D).

Besides its morphology and structure, the formation process of the sea-urchin shaped Bi$_2$S$_3$/CdS hierarchical heterostructure through the one-pot process is also worth exploring. In order to reveal the growth mechanism of the Bi$_2$S$_3$/CdS hierarchical heterostructure in more detail, time-dependent experiments were carried out and the resulting products were analyzed by SEM. Fig. 6A–D presents a series of SEM images of the products obtained at different reaction times. As shown in Fig. 6A, at the early reaction stage (5 min), the product was only flower-like Bi$_2$S$_3$ (about 1.2 μm). By prolonging the reaction time to 1 h, the Bi$_2$S$_3$ nanoflowers became larger with a diameter of about 1.5 μm (Fig. 6B). The nanoflowers were composed of nanorods with smooth surface. As the reaction proceeded (Fig. 6C), Cd^{2+} and S^{2-} gradually crystallized into CdS nanoparticles on the surface of Bi$_2$S$_3$ nanoflowers to form hierarchical structure through the nucleation-aggregation deposition process. Ultimately, perfect sea-urchin shaped Bi$_2$S$_3$/CdS hierarchical heterostructures with an average size of about 1.5 μm were formed after the reaction was carried out for 10 h (Fig. 6D).

Based on the above results, the possible growth pattern and formation mechanism of sea-urchin shaped Bi$_2$S$_3$/CdS hierarchical heterostructure is shown in scheme 1. At elevated reaction temperature, thiourea hydrolyzed to release H$_2$S with the assistance of a trace amount of the mixture of ethanol and

glycerol. According to the K_{sp} of Bi_2S_3 (1.0×10^{-97}) and CdS (8.0×10^{-27}),[39] it is expected that Bi_2S_3 will preferentially deposit and form sea-urchin shaped nanoflowers (crystal seeds) inside the autoclave before CdS, Bi^{2+} and glycerol first to form flower-like

5   ligand. However, in the reaction system, the positively charged ions, such as Cd^{2+} and so forth, could weaken the activation energy of the surface of the Bi_2S_3 nanoflowers, which would provide many high energy sites for further growth and promote their desorption from the surface of nanoflowers,[36,40,41] so leading

10 to the following growth of CdS nanoparticles. When Bi^{3+} was depleted, the nucleation process of CdS was initialized. Further extending the reaction time, a larger number of Cd^{2+} ions in the solution could get enough energy to nucleation onto the surface of the Bi_2S_3 nanoflowers. Along with the prolonged reaction time,

15 numerous CdS nanoparticles are uniformly coated on the surface of the Bi_2S_3 nanoflowers. Eventually, the sea-urchin shaped Bi_2S_3/CdS hierarchical heterostructures were formed (Fig. 6 D).
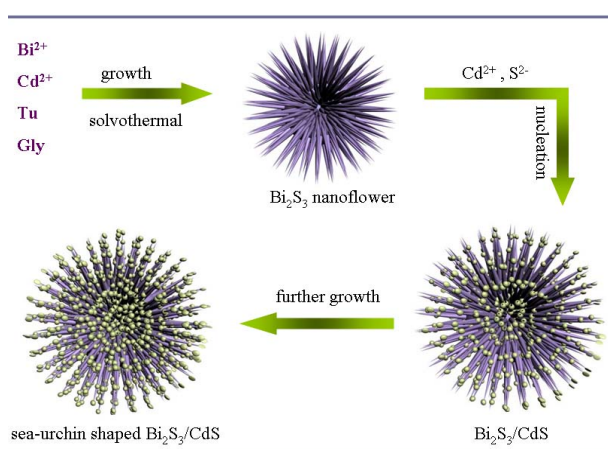
20 **Scheme 1** Illustration of the morphological evolution process of the sea-urchin shaped Bi_2S_3/CdS hierarchical heterostructures (BC2).
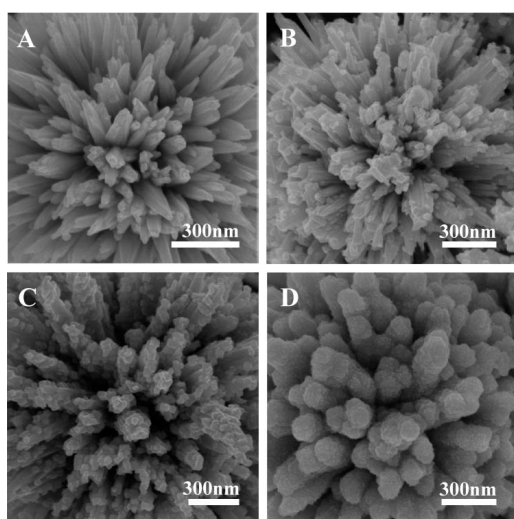
**Fig. 7** SEM images of samples with different molar ratios of Bi_2S_3 and
25 CdS: (A) BC5, (B) BC3, (C) BC2, (D) BC1.

In order to further study the optimal structure of the heterostructures, we also prepared Bi_2S_3/CdS composites with various CdS contents. For different molar ratio (5:1, 3:1, 2:1 and 1:1) of $Bi(NO_3)_3 \cdot 5H_2O$ and $Cd(NO_3)_2 \cdot 4H_2O$, the resulting

30 samples were labeled as BC5, BC3, BC2, BC1. Surprisingly, significant differences in surface roughness are observed from SEM images of the various Bi_2S_3/CdS samples in Fig. 7A-D. It can be seen that, with the increase of the amount of $Cd(NO_3)_2 \cdot 4H_2O$, the amount of CdS nanoparticles decorated on

35 the Bi_2S_3 surface increased gradually, and when the amount is too much, the surface of Bi_2S_3 nanoflowers was completely coated by CdS nanoparticles (Fig. 7D). This is not conducive to improve charge transport and enhance the electron-hole separation. Therefore, proper CdS coverage degree is necessary.

40 The photocatalytic activities of the sea-urchin shaped Bi_2S_3/CdS hierarchical heterostructures with different CdS contents were evaluated by the degradation of rhodamine B (RhB) in aqueous solution under visible-light irradiation. In order to prove the synergetic effect of the hybrid structure, the control

45 photocatalytic experiments of Bi_2S_3 alone and CdS alone were also performed. Before the photocatalytic reaction, the dark adsorption experiments were performed, and the concentrations of RhB almost do not change under dark conditions after the adsorption–desorption equili-brium (60 min). Meanwhile, the

50 RhB solutions were also photolyzed in the absence of the photocatalysts to examine their stability, and the dyes are not decomposed even after long illumination with visible light. Therefore, the presence of both catalysts and visible light illumination is necessary for efficient degradation. As can be seen

55 from Fig. 8, C is the concentration of RhB after visible light irradiation for a certain period, and C_o is the concentration of the RhB after reaching adsorption/desorption equilibrium in dark. Pure Bi_2S_3 sample shows low visible-light photocatalytic activity, and about 40% of RhB is degraded within 80 min. The

60 photocatalytic activity of an individual CdS is also relatively low (about 50% of RhB is degraded within 80 min). In contrast, considerable high activity is recorded for Bi_2S_3/CdS samples, especially BC2 exhibits the highest visible-light photocatalytic activity, and almost all of RhB is degraded within 80 min, which

65 exceeds that of pure Bi_2S_3 and CdS samples. The reason of the excellent photocatalytic activity is due to the synergetic effect of hierarchical flower-like structure and the improved charge carrier separation process. First, hierarchical flower-like structure can contribute to the effective utilization of visible light by multiple

70 reflections and materials transportation.[10,42] Second, it is believed that effective separation of photogenerated electron/hole pairs is crucial in enhancing the photocatalytic activity of Bi_2S_3/CdS composites. To demonstrate the structure-induced enhancement of the photocatalytic performance of the sea-urchin shaped

75 Bi_2S_3/CdS hierarchical heterostructure composite, the control samples, the crushed Bi_2S_3/CdS composite nanoparticles (Fig. S1) were also used as photocatalysts. The Bi_2S_3/CdS hierarchical heterostructure composite exhibit higher photocatalytic activity than the corresponding crushed one (Fig. S2). The enhanced

80 photocatalytic activity can be attributed to its special structural features. The sea-urchin shaped hierarchical superstructure can allow multiple reflections of visible light, which enhances light-harvesting and thus increases the quantity of photogenerated electrons and holes available to participate in the photocatalytic

85 degradation of RhB.[34] Meanwhile, the sea-urchin shaped

hierarchical superstructure can provide transport circumstances for reactant substances of different size, and expedite mass transportation, so the chemical reactions can happen more easily.[43,44]
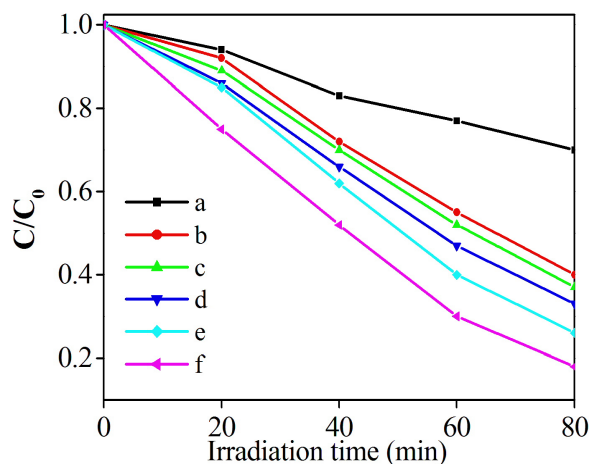
Fig. 8 Comparison of photocatalytic degradation of RhB aqueous solutions (10 mg/L) degraded by (a) Bi_2S_3, (b) BC5, (c) CdS, (d) BC1,(e) BC3, and (f) BC2 under visible light irradiation.

In our study, there exists intimate contact between Bi_2S_3 and CdS in the Bi_2S_3/CdS hierarchical heterostructures. The interface between the two phases can act as a rapid separation site for the photogenerated electrons and holes due to the difference in the energy levels of their conduction bands (CB) and valence bands (VB). As shown in Fig. 9A, the band gap of CdS and Bi_2S_3 is about 2.42 eV and 1.38 eV, respectively. The conduction band of Bi_2S_3 is lower than that of CdS. Upon irradiation, electrons are promoted from the valence bands of CdS and Bi_2S_3 to their respective conduction bands. The photogenerated electrons easily migrate from the conduction band of CdS to that of the Bi_2S_3, creating positive holes in the valence band of CdS. Meanwhile, holes in the valence band of CdS transfer to that of Bi_2S_3. Since the E_{CB} potential of Bi_2S_3 (−0.76 eV vs NHE) is more negative than E_0 (O_2/·O_2-) (−0.046 eV vs NHE), the electrons left on the E_{CB} of Bi_2S_3 could reduce O_2 to ·O_2- through one-electron reducing reaction.[36] The unstable ·O_2- reacts with water quickly, producing hydroxyl (•OH) radicals. Meanwhile, the holes at the surfaces of CdS nanoparticles can react directly with surface H_2O molecules or OH⁻ in the solution to generate hydroxyl (•OH) radicals, which is a strong oxidizing agent to decompose RhB.[45] Although the photochemical reactions taking place at the surface of the photocatalyst are relatively slower compared to the interface charge transfer processes, they help reduce the recombination of the photogenerated charge carriers and lead to the high efficiency of the photocatalyst.[36] All the radicals can react with organic chemicals in the solution and improve the photoactivity. In order to prove the photocatalytic reaction mechanism in this system, it is important to detect hydroxyl radicals (•OH), which is the primary oxidant in the photocatalytic system. In this study, the formation of •OH on the surface of photocatalysts was detected by the fluorescence technique (PL) using terephthalic acid (TA) as a probe molecule because TA reacts with •OH in basic solution to generate 2-hydroxy-

terephthalic acid (TAOH), which emits a unique fluorescence signal with the peak centered at 426 nm.[46] Fig. 9B shows the typical PL spectral observed during visible-light irradiation in the system of catalyst and terephthalic acid. It can be clearly seen that the maximum emission intensity in fluorescence spectra was recorded at 425 nm by the excitation at about 315 nm, and the maximum number of •OH radicals is formed by using the Bi_2S_3/CdS heterostructure composite in the photoreaction process. Generally, the fluorescence intensity of TAOH is proportional to the amount of •OH produced on the surface of photocatalysts, and the photocatalytic activity has a positive correlation with the formation rate of •OH radicals.[47] Therefore, this result is in good agreement with the result of photodegradation of RhB.
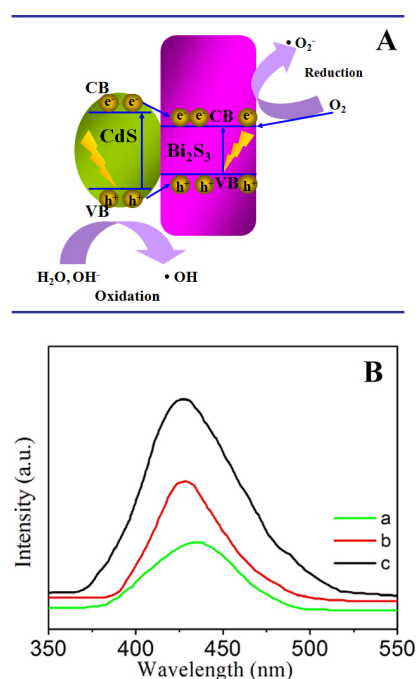
Fig. 9 (A) Schematic illustration showing the reaction mechanism for photocatalytic degradation of organic pollutants over the Bi_2S_3/CdS heterostructure composite. (B) Fluorescence spectra of TAOH (2-hydroxyterephthalic acid) formed by the reaction of terephthalic acid (5×10^{-4} M, excitation at 315 nm) with •OH radicals in the presence of different samples under visible-light irradiation for 20 min, Bi_2S_3 (a), CdS (b) and Bi_2S_3/CdS heterostructure composite (c).

In addition, the amount of CdS has obvious influence on the photocatalytic ability in the present composite system (Fig. 8). When the amount of CdS is relatively low (BC5), the Bi_2S_3/CdS nanostructure provides relatively low surface active sites. Increase the amount of CdS (BC2), the degradation rates of RhB reached the maximum value (82%, Fig. 8 f). However, excess CdS content also reduced the catalytic efficiency of the Bi_2S_3/CdS composite (BC1, Fig. 8 b), suggesting that a too high content of CdS was unfavorable to the degradation of RhB owing to the increased recombination of excited electrons and holes. These systematic changes further demonstrate the favorable role of the efficient separation of photogenerated electron-hole pairs by the combination of Bi_2S_3 and CdS in the hierarchical heterostructures in the preferential degradation of RhB. In addition, the sea-urchin shaped hierarchical superstructure (BC2)

can allow multiple reflections of visible light, which enhances light-harvesting and thus increases the quantity of photogenerated electrons and holes available to participate in the photocatalytic degradation of RhB.[34]
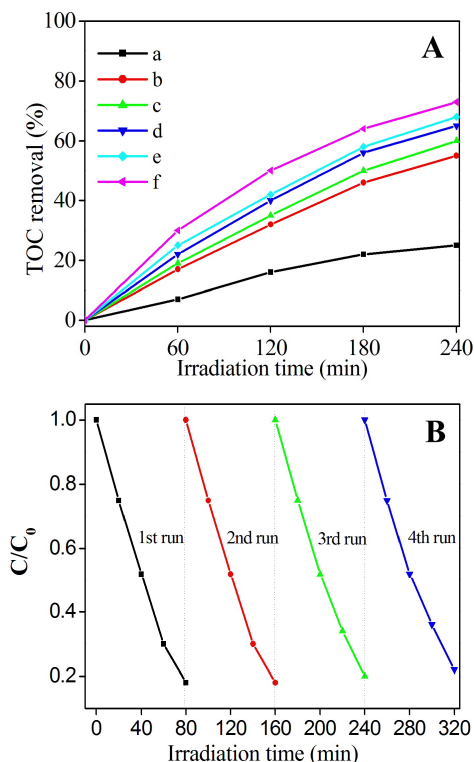
Fig. 10 (A) The profiles of total organic carbon (TOC) removals for the photodegradation of RhB (10 mg/L) in different aqueous catalysts under visible light irradiation, (a) Bi_2S_3, (b) BC5, (c) CdS, (d) BC1,(e) BC3, and (f) BC2. (B) Repeated photocatalytic test of RhB over recycled Bi_2S_3/CdS heterostructure composite (BC2) under visible light irradiation.

In semiconductor photocatalytic process, lots of studies showed that some degradation intermediates may be more toxic than the initial materials. Hence, the complete mineralization of dye components prior to wastewater discharging is important. To further investigate the mineralization degree of RhB, the total organic carbon (TOC) removal during the degradation of RhB by Bi_2S_3/CdS heterostructure composite under visible-light irradiation was tested. From Fig. 10A, it can be seen that TOC removal efficiency of Bi_2S_3/CdS heterostructure composite is 49.2% for RhB after 240 min, which is higher than that of the Bi_2S_3 and CdS. This results showed that, for the Bi_2S_3/CdS hierarchical heterostructure composite, a larger degree of light-generated hole/electron pair excitation produced, leading to the generation of more •OH radicals, and in turn, greater pollutant mineralization. Moreover, TOC removal efficiency of the Bi_2S_3/CdS hierarchical heterostructure composite also exhibit higher than that of the corresponding crushed one (Fig. S3), which is in agreement with the result of the photocatalytic test (Fig. S2). It further proves the obtained Bi_2S_3/CdS hierarchical heterostructure composite show strongly structure-induced enhancement of photocatalytic performance for the photodegradation of RhB.

In addition to photocatalytic activity, for a metal sulfide photocatalyst to be commercially viable, the stability is another important issue for their practical applications. In our experiment, the stability of the Bi_2S_3/CdS heterostructure (BC2) was evaluated by performing the cycling experiments under the same conditions. As shown in Fig. 10B, the Bi_2S_3/CdS heterostructure composite (BC2) does not exhibit evident loss of activity after four recycles, indicating the good stability. The high stability of the Bi_2S_3/CdS heterostructure composite is attributed to the close interaction between Bi_2S_3 and CdS, which favors the transfer of the photogenerated holes from the value band (VB) of CdS to the value band (VB) of Bi_2S_3, so effectively preventing the photocorrosion of CdS, as shown in Fig. 9A. Meanwhile, the photogenerated electrons can also be easily transferred from the conduction band of CdS to Bi_2S_3 conduction band. The separated holes and electrons can react with adsorbed water and oxygen to form various strong oxidizing species, which can decompose RhB. Therefore, the migration and separation of photogenerated electrons and holes effectively improved the stability of Bi_2S_3/CdS composites under light irradiation.

4. Conclusions

In summary, we have successfully prepared sea-urchin shaped Bi_2S_3/CdS hierarchical heterostructures via one-pot controlled hydrothermal method without any templates or surfactants. Experimental results proved that reaction time and the molar ratio of the reactants played an important role in the formation of sea-urchin shaped Bi_2S_3/CdS hierarchical heterostructures. The as-prepared Bi_2S_3/CdS heterostructures showed significantly structure-induced enhancement of photocatalytic performance for the degradation of RhB in aqueous solution due to the hierarchical heterostructures and the synergistic activity of CdS nanoparticles and Bi_2S_3 nanoflowers. The inherent characteristics of Bi_2S_3/CdS heterostructures may open up the prospect to understand and modify other semiconductor materials.

Acknowledgments

Notes

[a] Key Laboratory of Functional Inorganic Material Chemistry, Ministry of Education of the People's Republic of China, Heilongjiang University, Harbin 150080 P. R. China
[b] Key Laboratory of Chemical Engineering Process & Technology for High-efficiency Conversion, College of Heilongjiang Province, School of Chemistry and Materials Science, Heilongjiang University, Harbin 150080, China.

Corresponding author E-mail: tiangh@hlju.edu.cn, Tel.: +86 451 8660 4330, Fax: +86 451 8667 3647

References

1. (a) G. H. Tian, Y. J. Chen, R. T. Zhai, J. Zhou, W. Zhou, R. H. Wang, K. Pan, C. G. Tian and H. G. Fu. *J. Mater. Chem.*, A, 2013, **1**, 6961; (b) Z. Q. Liu, W. Y. Huang, Y. M. Zhang and Y. X. Tong. *CrystEngComm*, 2012, **14**, 8261; (c) S. Stankovich, D. A. Dikin, G. H. B. Dommett, K. M. Kohlhaas, E. J. Zimney, E. A. Stach, R. D.Piner and S. T. Nguyen, *Nature*, 2006, **442**, 282; (d) W. Gao, L. B. Alemany, L. Ci and P. M. Ajayan, *Nat. Chem.*, 2009, **1**, 403; (e) A. C. Balazs, T. Emrick, T. P. Russell, *Science*, 2006, **314**, 1107; (f) R. Bashyam, P. Zelenay, *Nature*, 2006, **443**,63; (g) J. R. Capadona, O. Van Den Berg, L. A. Capadona, M. Schroeter, S. J. Rowan, D. J. Tyler and C. Weder, *Nat. Nanotechnol*, 2007, **2**, 765; (h) X. Huang, X. Y. Qi, F. Boey and H. Zhang, Chem. *Soc. Rev.*, 2012, **41**, 666; (i) Q. Y. He, S. X. Wu, Z. Y. Yin. and H. Zhang, *Chem. Sci.*, 2012, **3**, 1764.

2. Z. Wang, J. G. Hou, C. Yang, S. Q. Jiao and H. M. Zhu, *Chem. Commun.*, 2014, **50**, 1731.

3. L. Huang, X. L. Wang, J. H. Yang, G. Liu, J. F. Han and C. Li, *J. Phys. Chem. C.*, 2013, **117**, 11584.

4. H. J. You, R. Liu, C. C. Liang, S. C. Yang, F. Wang, X. G. Lu and B. J. Ding, *J. Mater. Chem. A.*, 2013, **1**, 4097.

5. H. W. Park, W. Y. Choi and M. R. Hoffmann, *J. Mater. Chem.*, 2008, **18**, 2379.

6. H. Tong , S. X. Ouyang, Y. P. Bi, N. Umezawa, M. Oshikiri and J. H. Ye, *Adv. Mater.*, 2012, **24**, 229.

7. Y. Shi, H. Y. Li, L. Wang, W. Shen and H. Z. Chen, *ACS Appl. Mater. Interfaces*, 2012, **4**, 4800.

8. Z. R. Tang, X. Yin, Y. H. Zhang and Y. J. Xu, *Inorg. Chem.*, 2013, **52**, 11758.

9. Q. J. Xiang, J. G. Yu and M. Jaroniec, *J. Am. Chem. Soc.*, 2012, **134**, 6575.

10. J. Zhou, G. H. Tian, Y. J. Chen, Y. H. Shi, C. G. Tian, K. Pan and H. G. Fu, *Sci. Rep.,* DOI: 10. 1038/ srep 04027.

11. Z. Y. Ren , J. Y. Zhang , F. X. Xiao and G. C. Xiao, *J. Mater. Chem. A*, 2014, **2**, 5330.

12. L. G. Gai, X. Q. Duan, H. H. Jiang, Q. H. Mei, G. W. Zhou, Y. Tian and H. Liu, *CrystEngComm*, 2012, **14**, 7662.

13. Y. L. Min, G. Q. He, Q. J. Xu and Y. C. Chen, *J. Mater. Chem. A,* 2014, **2**, 2578.

14. L. J. Zhang, T. F. Jiang, S. Li, Y. C. Lu, L. L. Wang, X. Q. Zhang, D. J. Wang and T. F. Xie, *Dalton Trans*., 2013, **42**, 12998.

15. (a) X.-Y. Chen, T. Ling and X.-W. Du, *Nanoscale*, 2012, **4**, 5602. (b) J. Fang, L. Xu, Z. Y. Zhang, Y. P. Yuan, S. W. Cao, Z. Wang, L. S. Yin, Y. S. Liao and C. Xue, *ACS Appl. Mater. Interfaces,* 2013, **5**, 8088.

16. X. F. Wang, S. F. Li, Y. Q. Ma, H. G. Yu and J. G. Yu, *J. Phys. Chem. C*, 2011, **115**, 14648.

17. Q. Zhu, W. S. Wang, L. Lin, G. Q. Gao, H. L. Guo, H. Du and A. W. Xu, *J. Phys. Chem. C*, 2013, **117**, 5894.

18. (a) Z. W. Mei, S. X. Ouyang, D.-M. Tang, T. Kako, D. Golbergc and J. H. Ye, *Dalton Trans*., 2013, **42**, 2687. (b) Z. F. Liu, Z. G. Zhao and M. Miyauchi, *J. Phys. Chem. C*, 2009, **113**, 17132.

19. S. He,a G.-S. Wang, C. Lu, J. Liu, B. Wen, H. Liu, L. Guo and M.-S. Cao, *J. Mater. Chem. A*,, 2013, **1**, 4685.

20. C. Murray, C. Kagan and M. Bawendi, *Annu. Rev. Mater. Sci.*, 2000, **30**, 545.

21. Y. N. Xia, P. D. Yang, Y. G. Sun, Y. Y. Wu, B. Mayers, B. Gates, Y. D. Yin, F. Kim and H. Q. Yan, *Adv. Mater.*, 2003, **15**, 353.

22. N. Z. Bao, L. M. Shen, T. Takata, K. Domen, *Chem. Mater.*, 2008, **20**, 110.

23. G. J.Ma, H. J. Yan, J. Y. Shi, X. Zong, Z. B. Lei and C. Li, *J. Catal.*, 2008, **260**, 134.

24. N. Buhler, K. Meier and J. F. Reber, *J. Phys. Chem.*, 1984, **88**, 3261.

25. H. J. Yan, J. H. Yang, G. J. Ma, G. P. Wu, X. Zong, Z. B. Lei, J. Y. Shi and C. Li, *J. Catal.*, 2009, **266**, 165.

26. (a) Y. H. Zhang, N. Zhang, Zi-R. Tang and Y.-J. Xu, *Chem. Sci.*, 2012, **3**, 2812. (b) J. Y. Zhang, Y. H. Wang, J. Jin, J. Zhang, Z. Lin, F. Huang and J. G. Yu, *ACS Appl. Mater. Interfaces*, 2013, **5**, 10317.

27. S. R. Luo, F. Chai, L. Y. Zhang, C. G. Wang, L. Li, X. C. Liu and Z. M. Su, *J. Mater. Chem.*, 2012, **22**, 4832.

28. J. H. Kim, H. Park, C. H. Hsu and J. Xu, *J. Phys. Chem. C*, 2010, **114**, 9634.

29. J. M. Ma, Z. F. Liu, J. B. Lian, X. C. Duan, T. Kim, P. Peng, X. D. Liu, Q. Chen, G. Yao and W. J. Zheng, *CrystEngComm*, 2011, **13**, 3072.

30. Q. Han, J. Chen, X. Yang, L. Lu and X. Wang, J. Phys. Chem. C, 2007, 111, 14072; W. Lou, M. Chen, X. Wang and W. Liu, *Chem. Mater.*, 2007, **19**, 872.

31. (a) J. Xu, N. Petkov, X. Wu, D. Lacopino, A. J. Quinn, G. Redmond, T. Besin, M. A. Morris and J. D. Holmes,*ChemPhysChem*, 2007, **8**, 235; (b) H. Bao, C. M. Li, X. Cui, Y. Gan, Q. Song and J. Guo, *Small*, 2008, **4**, 1125.

32. D. Wang, C. Hao, W. Zheng, X. Ma, D. Chu, Q. Peng and Y. Li, *Nano Res.*, 2010, **2**, 130.

33. Y. Zhao, Y. Xie, J. S. Jie, C. Y. Wu and S. Yan, *J. Mater. Chem.*, 2009,**19**, 3378.

34. Y. Wang, J. Chen, L. Chen, Y. B. Chen and L. M. Wu, *Cryst. Growth. Des.*, 2010, **10**, 1578.

35. X. B. He, L. Gao, S. W. Yang and J. Sun, *CrystEngComm*, 2010, **12**, 3413.

36. Z. Fang, Y. F. Liu, Y. T. Fan, Y. H. Ni, X. W. Wei, K. B. Tang, J. M. Shen, and Y. Chen, *J. Phys. Chem. C*, 2011, **115**, 13968.

37. B. Zhang, X. C. Ye, W. Y. Hou, Y. Zhao and Y. Xie, *J. Phys. Chem. B*, 2006, **110**, 8978.

38. J. Grigas, E. Talik and V. Lazauskas, *Phys. Status. Solidi. B*, 2002, **232**, 220.

39. T. N. Knoxville and A. D. John, *Lange＇s Handbook of Chemistry*, ed. McGraw-Hill, Inc.:New York, 1999.

40. A. Z. Zelikin, G. K. Such, A. Postma and F. Caruso, *Biomacromolecules*, 2007, **8**, 2950.

41. J. G. Yu, L. J. Zhang, B. Cheng and Y. R. Su, *J. Phys. Chem. C*, 2007, **111**, 10582.

42. J. Zhou, G. H. Tian, Y. J. Chen, J. Q. Wang, X. R. Cao, Y. H. Shi, K. Pan and H. G. Fu, *Dalton Trans.*, 2013, **42**, 11242.

43. J. G. Yu, G. P. Dai and B. B. Huang, *J. Phys. Chem. C*, 2009, **113**, 16394.

44. D. R. Rolison, *Science*, 2003, **299**, 1698.

45. A. Yamakata, T. Ishibashi and H. Onishi, *J. Phys. Chem. B*, 2001, **105**, 7258.

46. S. Khanchandani, S. Kundu, A. Patra and A. K. Ganguli, *J. Phys. Chem. C*, 2013, **117**, 5558.

47. Z. J. Li, J. J. Wang, X. B. Li, X. B. Fan, Q. Y. Meng, K. Feng, B. Chen, C. H.Tung and L. Z. Wu, *Adv. Mater.*, 2013, **25**, 6613.